

Supporting Information for

Tailoring Surface Reaction Pathway by Self-Assembling Trifluoromethyl-Terminated Molecular Layer to Enhance Photocatalytic Cellulose-to-Syngas Conversion in Pure Water

Jianfeng Lin¹, Ren Yu^{1,2}, Xiaoyu Shi¹, Jie Zhao¹, Shangxian Chen¹, Liang Huang¹, Libo Li³, Donglei Bu^{1*}, Ning Cai^{1,2*}, Shaoming Huang^{4*}

¹School of Materials and Energy, Guangzhou Key Laboratory of Low-Dimensional Materials and Energy Storage Devices, Guangdong University of Technology, Guangzhou 510006, P. R. China

²School of Chemical Engineering and Light Industry, Guangdong University of Technology, Guangzhou 510006, China

³School of Chemistry and Chemical Engineering, Guangdong Prov Key Lab Green Chem Prod Technol, South China University of Technology, Guangzhou 510640, PR China

⁴School of Chemistry and Materials Science, Hangzhou Institute for Advanced Study University of Chinese Academy of Sciences, Hangzhou, 310024, P. R. China

Email: budonglei@gdut.edu.cn, ning.cai@gdut.edu.cn, smhuang@gdut.edu.cn

Experimental Section:

Materials:

2-Methylimidazole (2-MiM), hexadecyl trimethyl ammonium Bromide (CTAB), $\text{Zn}(\text{CH}_3\text{COO})_2 \cdot 2\text{H}_2\text{O}$, chloroplatinic acid, sodium borohydride, titanium (IV) butoxide, methanol, selenium were commercial available and used as received.

Synthesis of Poz3F:

Methyl 4-(3,7-bis(4-(trifluoromethyl)phenyl)-10H-phenoxazin-10-yl)benzoate:
Compound 1 methyl 4-(3,7-dibromo-10H-phenoxazin-10-yl)benzoate (0.475 g, 1.00 mmol), 4-Trifluoromethylphenylboronic acid (0.475 g, 2.50 mmol), potassium carbonate (2 M, 6.0 mL), and tetrahydrofuran were added to the reaction flask to fully stir and dissolve and the gas was pumped three times, Tetrakis (triphenylphosphine) palladium (23.10 g, 0.20 mmol) was added in a nitrogen atmosphere and reacted at 70 °C overnight to obtain compound, and finally water was added to stop the reaction, and dichloromethane was extracted. The organic layer was washed three times with water and brine, dried with anhydrous sodium sulfate, the solvent was removed by rotary evaporation, and purified with petroleum ether/ethyl acetate (volume ratio = 15/1) as an eluent to obtain 2 0.47 g (77%) of yellow solid. ^1H NMR (400 MHz, Chloroform-d) δ 8.32 (d, J = 8.5 Hz, 2H), 7.64 (d, J = 8.3 Hz, 4H), 7.58 (d, J = 8.2 Hz, 4H), 7.49 (d, J = 8.5 Hz, 2H), 7.02 (d, J = 2.1 Hz, 2H), 6.88 (dd, J = 8.3, 2.1 Hz, 2H), 6.03 (d, J = 8.3 Hz, 2H), 3.99 (s, 3H).

4-(3,7-bis(4-(trifluoromethyl)phenyl)-10H-phenoxazin-10-yl) benzoic acid: The compound formula 2 (0.605 g, 1.00 mmol) was dissolved in a mixed solution of MeOH/THF (the volume ratio of the two is 1:1), and then sodium hydroxide aqueous solution was added, stirred at 50 °C overnight, the reaction was gradually cooled to room temperature, the solution was concentrated under vacuum, acidified and filtered with 2M HCl, and 3 (Poz3F) 0.56 g (94%) of yellow solid was obtained after drying. ¹H NMR (400 MHz, DMSO-d₆) δ 13.28 (s, 1H), 8.26 (d, J = 8.0 Hz, 2H), 7.94–7.71 (m, 8H), 7.66 (d, J = 8.1 Hz, 2H), 7.22 (d, J = 2.1 Hz, 2H), 7.17–7.08 (m, 2H), 6.03 (d, J = 8.4 Hz, 2H).

Synthesis of Catalysts:

Synthesis of ZIF-8 particles: Typically, 0.74 mM CTAB was added to 5 mL of 2.72 M 2-MiM aqueous solution. Then, 5 mL of 0.273 M Zn(CH₃COO)₂·2H₂O aqueous solution was added into the mixed solution of 2-MiM and CTAB while stirring. The transparent mixture turned to milky within ~ 30 s. After two hours, the suspension was transferred to a Falcon tube and the ZIF-8 particles were washed three times with deionized water upon centrifuging at 9000 rpm, then dried at 80 °C.

Synthesis of ZIF-8/Pt: 150 mg ZIF-8 was added to 20 ml methanol. Then, 0.8 mL 0.0192 M chloroplatinic acid solution was added into the methanol dispersion of ZIF-8 while stirring. After two hours, 1 mg sodium borohydride was added into the mixed solution of ZIF-8 and chloroplatinic acid while stirring. After 10 min, the suspension was transferred to a Falcon tube and the ZIF-8/Pt particles were washed three times with methanol upon centrifugation at 9000 rpm, then dried at 80 °C.

Synthesis of ZIF-8/Pt@TiO₂: 150 mg ZIF-8/Pt and 0.6 mL deionized water was added to 60 mL methanol and then stirred for 30 min. A solution of titanium (IV) butoxide (Ti(OBu)₄, 0.3 ml, 0.5 ml, 0.7 ml or 0.9 ml in ethanol (total volume 6.0 mL) was then injected into the mixture using a syringe at a rate of 0.5 mL min⁻¹. Then the temperature was increased to 80 °C. After 90 min, the suspension was transferred to a Falcon tube and the ZIF-8/Pt@TiO₂ particles were washed three times with methanol upon centrifugation at 9000 rpm., then dried at 80 °C.

Synthesis of h-ZnO/Pt@TiO₂: 150 mg ZIF-8/Pt@TiO₂ was weighed in a crucible and heated to 550 °C at a rate of 5 °C/min and held for 2 hours in Air in a muffle furnace.

Synthesis of h-ZnSe/Pt@TiO₂: 50 mg ZnO/Pt@TiO₂ and 50 mg Selenium was weighed in a crucible and heated at 550 °C for 2 hours with a temperature increase of 5 °C/min in 5% H₂ + 95% Ar.

Synthesis of h-ZnSe/Pt@TiO₂-Poz3F: 100 mg h-ZnSe/Pt@TiO₂ was dispersed in a solution of Poz3F in DMF solvent for 240 min, followed by washing in DMF three times. The concentration of Poz3F solution was 1, 3, 5, 7, 10 mM.

Synthesis of ZnSe: The as obtained ZIF-8 was put in a crucible and heated to 550 °C at a rate of 5 °C/min and held for 2 hours in air in a muffle furnace. Then the obtained powder was mixed with Selenium in a crucible and heated at 550 °C for 2 hours with a temperature increase of 5 °C/min in 5% H₂ + 95% Ar.

Synthesis of TiO₂: The as obtained ZIF-8@TiO₂ was washed in 1 M HCl to remove ZIF-8. Then the TiO₂ were annealed at 550 °C for 2 hours in a muffle furnace

and then treated in 5% H₂ + 95% Ar with a temperature increase of 5 °C/min for 2 hours.

General Methods:

X-ray diffraction (XRD) measurements were carried out on a Rigaku Smartlab 9kW X-ray diffractometer. Scanning electron microscope (SEM) characterization was carried out on a Thermo Fisher Apero C scanning electron microscope. Transmission electron microscope (TEM) measurements were carried out on a FEI Talos F200S 200kV scanning/transmission electron microscope. Atomic force microscopy (AFM) measurements were carried out on a Multimode 8 AFM (Bruker, SO#47233). X-ray photoelectron spectroscopy (XPS) characterization was carried out on a Thermo Fisher Escalab 250Xi X-ray photoelectron spectrometer. Raman spectroscopy was carried out on a Renishaw plc Raman spectrometer. Electron paramagnetic resonance (EPR) measurements were performed on a Bruker A300 electron paramagnetic resonance instrument. The Ultraviolet–visible diffuse reflectance spectra were measured by a UV-vis spectrophotometer (Shimadzu UV-3600), and BaSO₄ was used as a reflectance standard material and the scanning range was 200-900 nm. The Fourier transform infrared spectra (FT-IR) of the samples were analyzed by infrared spectrometer (Nicolet IS50 Thermo fisher) using KBr disk. The Photo-luminescence (PL) spectrum was performed using a Fluorolog-3 fluorescence lifetime spectrophotometer. N₂ physisorption surface area using the Brunauer–Emmett–Teller (BET) method was recorded on a Micromeritics ASAP 2460 tool. Raman spectra (633 nm) were collected with Renishaw in via. Elemental analysis was performed on an Elementar: Vario EL

cube. Hall effect was measured by a Ecopia HMS-7000 Hall Effect measurement (measurement) System. The charge carrier mobility and sample resistance were measured using an Ecopia HMS-7000 Hall Effect Measurement System with the following parameters: test current: 1×10^{-10} A, magnetic field: 0.5 T, integration time: 20 s, and actual test time: 27 min.

All of the photoelectrochemical measurements were measured on a CHI 760E electrochemical station (Shanghai Chenhua, China) in ambient conditions. Generally, 3 mg of photocatalyst were dispersed in 1 mL 1% nafion ethanol solution. A glassy carbon electrode with a photocatalyst deposited served as the working electrode, while a platinum sheet and an Ag/AgCl electrode served as the counter and reference electrode, respectively. The electrolyte was a 0.2 M Na_2SO_4 solution and a 300 W Xe lamp was used as the visible light source. Determination of Soluble Compounds using an Agilent 1260 infinity HPLC system equipped with a refractive index detector (HPLC-RI) and a Rezex ROA-organic acid H^+ column (300×7.8 mm) to determine if soluble compounds (such as glucose and cellobiose) were present in the filtrate as a result of the pretreatment. The flow rate of the isocratic mobile phase (5 mM H_2SO_4) was set at 0.5 mL min^{-1} , and the RI and column temperatures were both $40 \text{ }^\circ\text{C}$.

Photocatalytic Cellulose Reforming Experiments

The time-dependent photocatalytic hydrogen production experiments were performed in Labsolar-6A online system (Beijing Perfectlight) at $5 \text{ }^\circ\text{C}$. A Xenon arc lamp (300 W) was employed as light source to trigger the photocatalytic reaction. The

photocatalyst and cellulose was dispersed in deionized water in the reaction cell by using a magnetic stirrer. Prior to the reaction, the mixture was degassed under vacuum to remove air. The generated gas phase products were characterized by Agilent 8860 gas chromatography (a molecular sieve 5A column, two Hayesep Q column, a thermal conductivity detector, a flame ionization detector, argon was used as carrier gas) connected with Perfectlight 6A system. The liquid phase products were tested using LC-MS (thermo scientific Q Exactive Ultimate 3000 UPLC). MS: Spray Voltage: 3200 V; Capillary Temperature: 300.00 °C; Sheath Gas: 40.00 Arb; Aux Gas: 8.00 Arb; Max Spray Current: 100.00 μ A; Probe Heater Temp.: 300.00 °C; Ion Source: ESI+/-ms. LC: column: ZORBAX SB-AQ 150 \times 4.6mm, 5 μ m Agilent; Temp.: 10 °C; u = 0.3 mL/min; Mobile phase: CH₃CN: 0.1% formic acid aqueous solution = 1:99.

Computational Details

The first-principles calculations are performed in the framework of the density functional theory with the projector augmented plane-wave method, as implemented in the Vienna ab initio simulation package.¹ The generalized gradient approximation of Perdew, Burke, and Ernzerhof (PBE) functional is employed for the exchange-correlation potential.² The long range van der Waals interaction is described by the DFT-D3 approach.³ The plane-wave basis with a kinetic energy cutoff of 500 eV and the Monkhorst-Pack scheme⁴ with a k-point grid spacing of $2\pi \times 0.04 \text{ \AA}^{-1}$, were employed to ensure convergence of the total energy. The converged conditions for ionic and electronic optimizations were chosen as 0.02 eV/ \AA and 1×10^{-5} eV, respectively. The adsorption energy E_{ads} is defined as: $E_{\text{ads}} = E_{\text{ad/sub}} - (E_{\text{ad}} + E_{\text{sub}})$, where

$E_{\text{ad/sub}}$, E_{ad} , and E_{sub} are the total energies of the adsorbate/substrate system, the adsorbate in the structure, and the clean substrate, respectively.

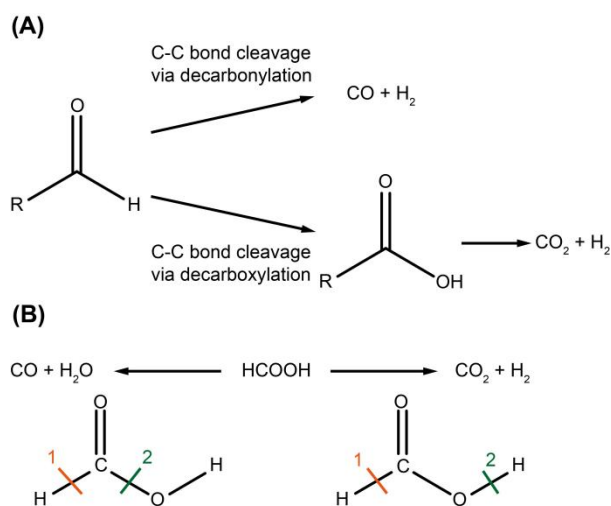


Figure S1. (A) Decarbonylation and decarboxylation pathway of sugar and (B) dehydrogenation and dehydration pathway of formic acid.

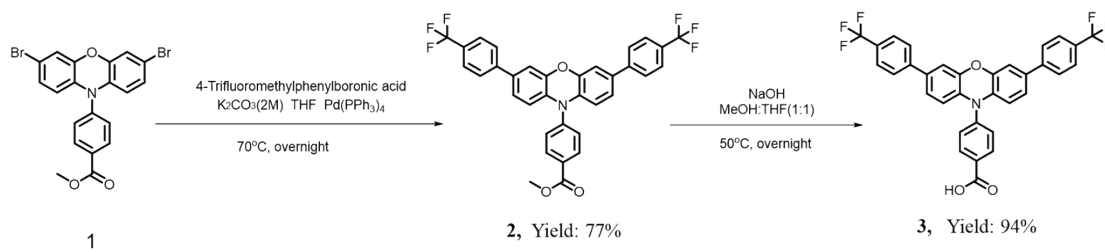


Figure S2. Synthetic route of Poz3F.

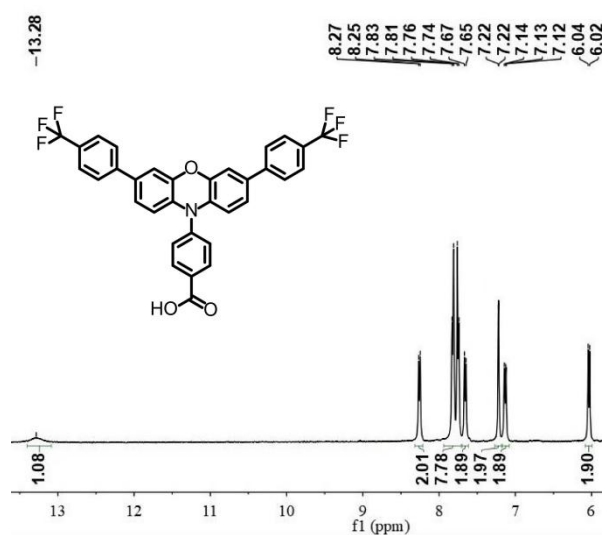


Figure S3. NMR spectrum of Poz3F.

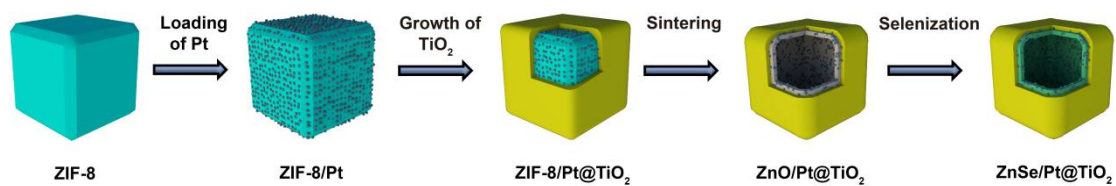


Figure S4. Schematic diagram displays the synthesis procedures of h-ZnSe/Pt@TiO₂ samples.

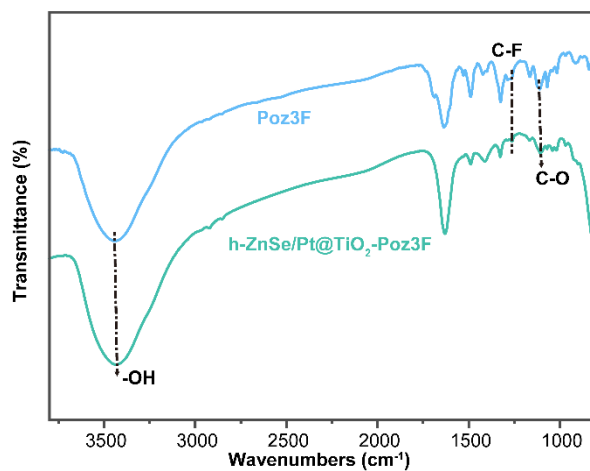


Figure S5. FT-IR spectra of Poz3F before and after adsorbed on h-ZnSe/Pt@TiO₂, respectively.

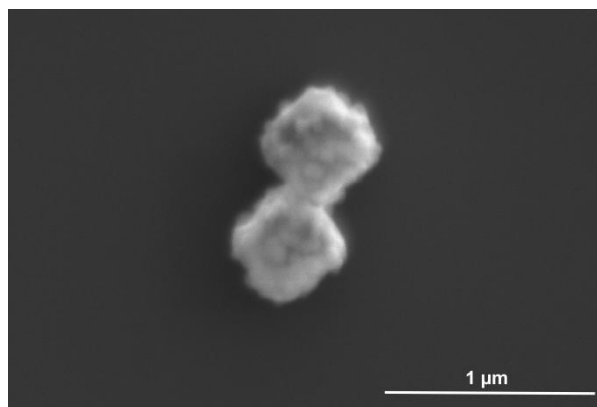


Figure S6. SEM image of h-ZnSe/Pt@TiO₂.

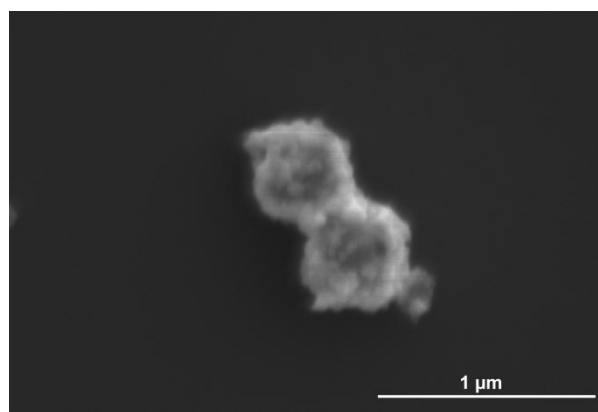


Figure S7. SEM image of h-ZnSe/Pt@TiO₂-Poz3F.

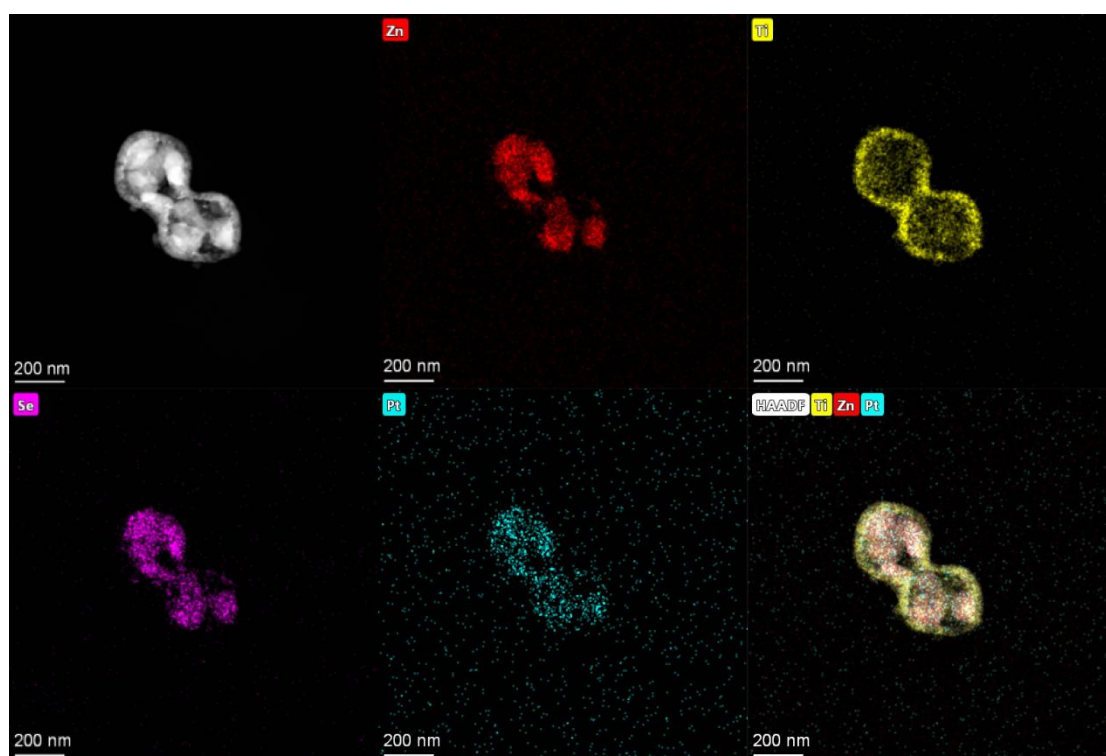


Figure S8. EDS mapping of SEM image of h-ZnSe/Pt@TiO₂. Zn: red, Ti: yellow, Se: purple, Pt: blue.

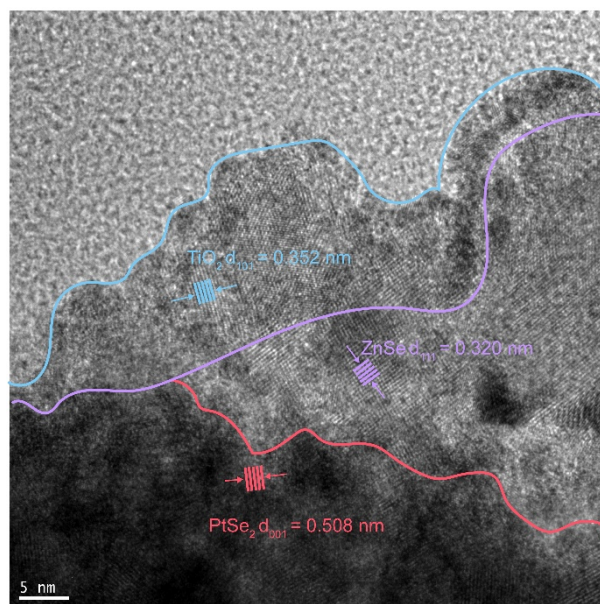


Figure S9. High-resolution TEM image of h-ZnSe/Pt@TiO₂.

Lattice fringes of ZnSe, TiO₂, and PtSe₂ are observed in the high-resolution TEM image. As revealed, the adjacent lattice spacing of 0.508 nm and 0.320 nm as shown in are corresponding to the (001) and (111) plane of PtSe₂ and ZnSe, respectively, showing the overlapped location of PtSe₂ and ZnSe. Additionally, lattice spacing of 0.352 nm corresponding to the (101) plane of TiO₂ is also observed next to ZnSe with distorted boundary, implying the heterojunction formation.

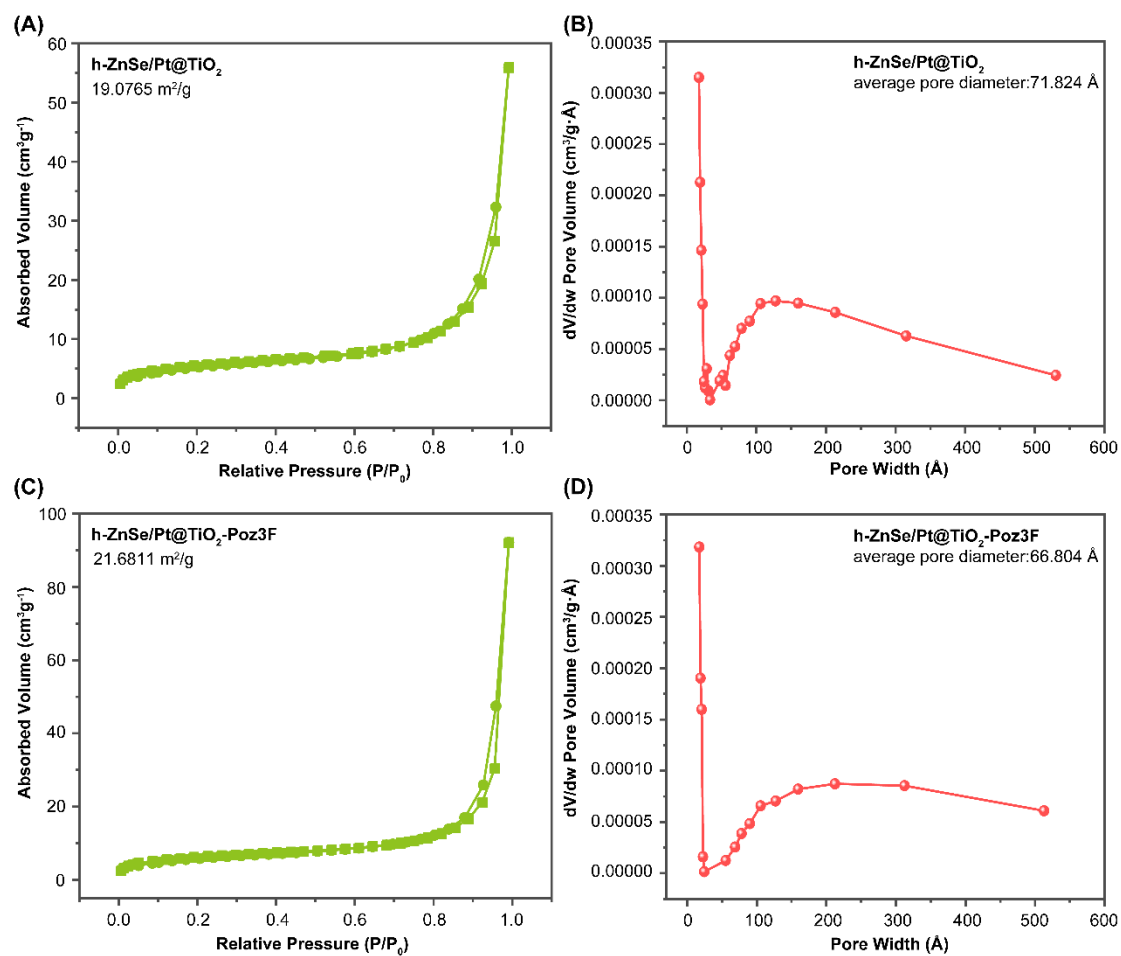


Figure S10. (A) Specific surface area and (B) pore distribution of h-ZnSe/Pt@TiO_2 , respectively. (C) Specific surface area and (D) pore distribution of $\text{h-ZnSe/Pt@TiO}_2\text{-Poz3F}$, respectively.

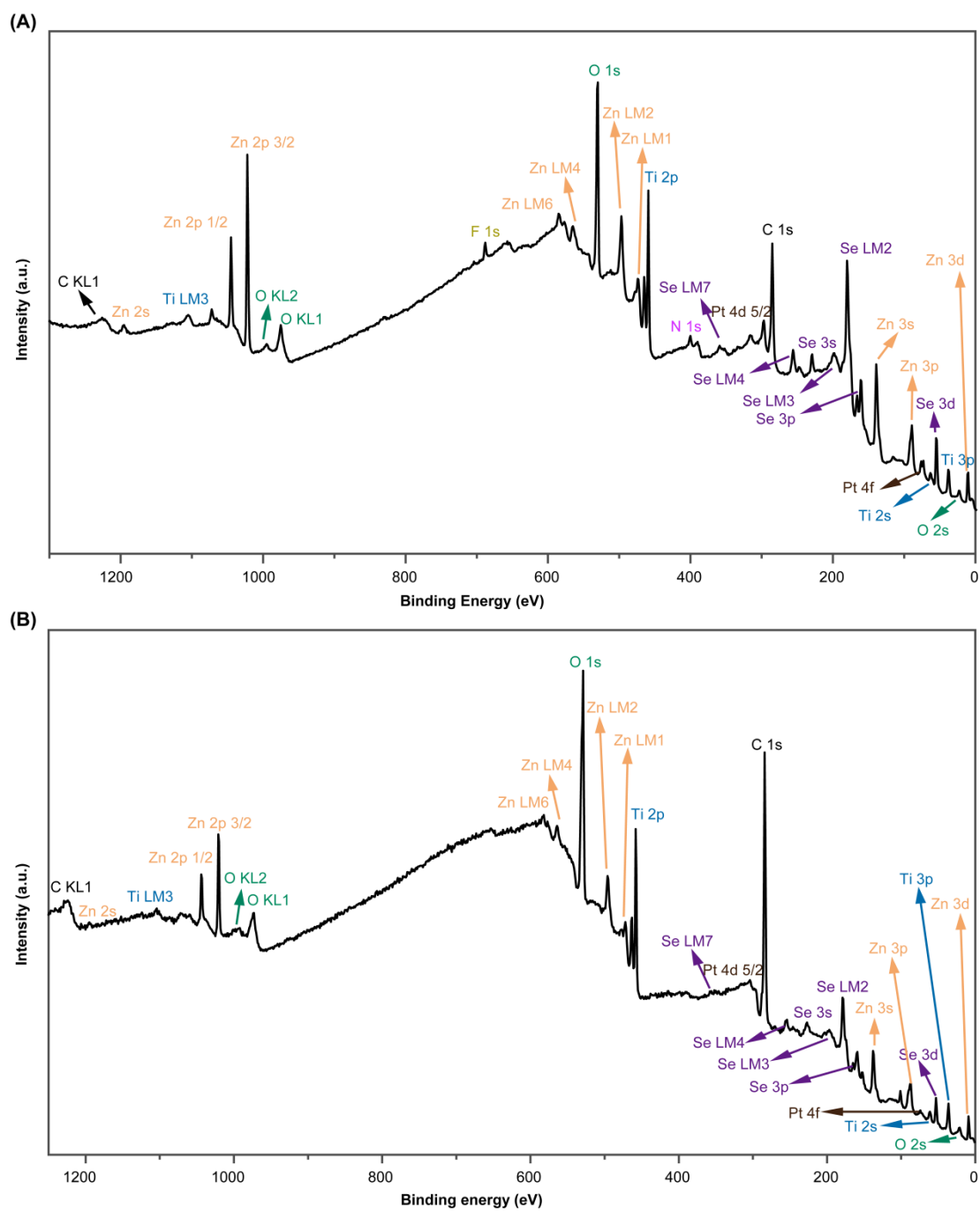


Figure S11. XPS full survey spectrum of (A) h-ZnSe/Pt@TiO₂-Poz3F and (B) h-ZnSe/Pt@TiO₂, respectively.

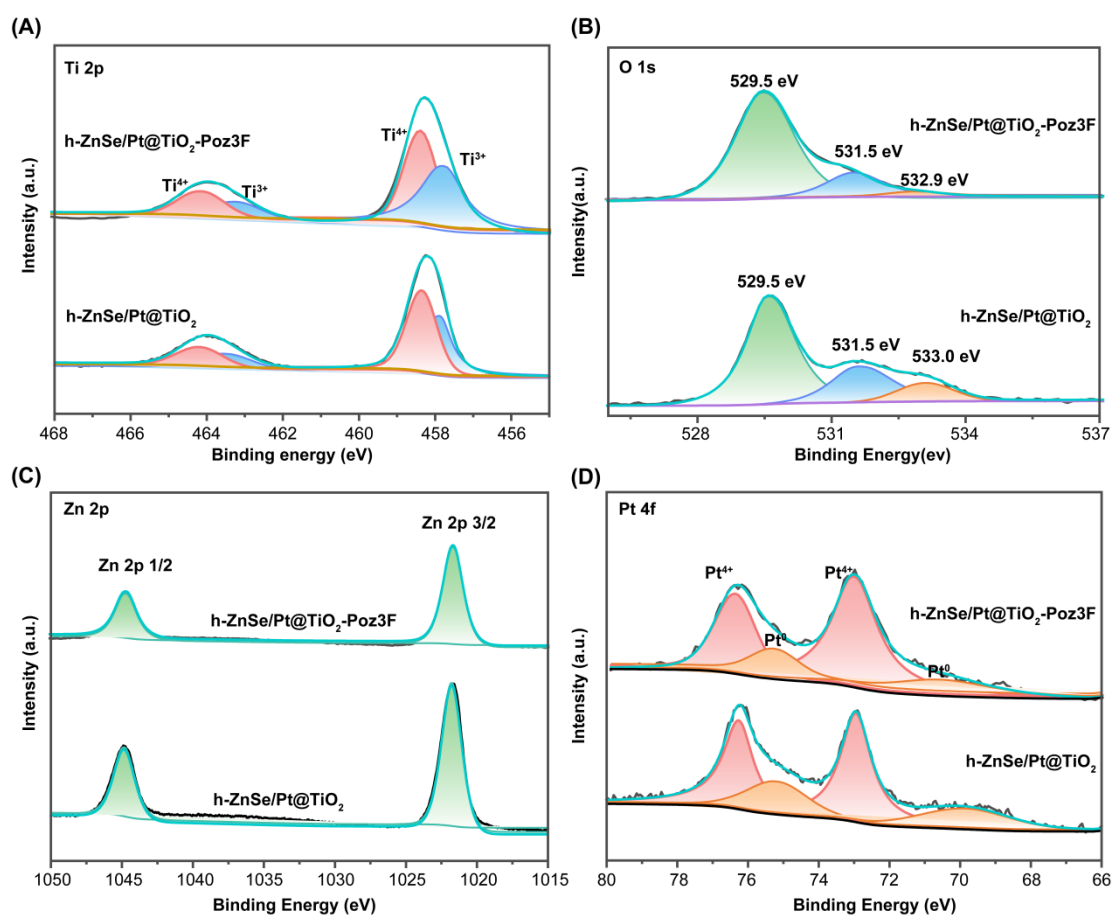


Figure S12. Narrow scan XPS spectra of (A) Ti 2p, (B) O 1s, (C) Zn 2p, (D) Pt 4f for h-ZnSe/Pt@TiO₂-Poz3F and h-ZnSe/Pt@TiO₂, respectively.

For both samples, four peaks were observed in the narrow scan Ti 2p XPS spectrum, which are located at 458.3, 457.9, 464.3, and 463.6 eV corresponding to the Ti⁴⁺ 2p_{3/2}, Ti³⁺ 2p_{3/2}, Ti⁴⁺ 2p_{1/2}, and Ti³⁺ 2p_{1/2}, respectively.⁵⁻⁶ The presence of Ti³⁺ on the surface indicates partial loss of the lattice oxygen, which can be further confirmed by the narrow scan O 1s XPS spectrum.⁵⁻⁶ Three peaks at with binding energies of 529.5, 531.5, and 533.0 eV related to the lattice oxygen, oxygen vacancies, and the O-H of surface hydroxyl group, respectively, were observed in the O 1s XPS spectra of both samples.⁵ Consistent with the observed Ti³⁺ species, oxygen vacancies also present in the samples, further confirming partial loss of the lattice oxygen. Two peaks at 1044.7 and 1021.7 eV ascribed to Zn²⁺ 2p_{1/2} and Zn²⁺ 2p_{3/2}, respectively, are identified

in both samples (Figure S10C).⁷⁻⁸ Narrow scan Pt 4f XPS in Figure S10D reveals that there are two chemical states of Pt, Pt⁴⁺ and Pt⁰, in both samples. Notably, the peak area corresponding to Pt⁴⁺ is much higher than that of Pt⁰, suggesting that the majority of Pt is in Pt⁴⁺ form. Additionally, the Pt⁴⁺ is like originated from PtSe₂ as revealed by the high-resolution TEM images (Figure 1D and S12).

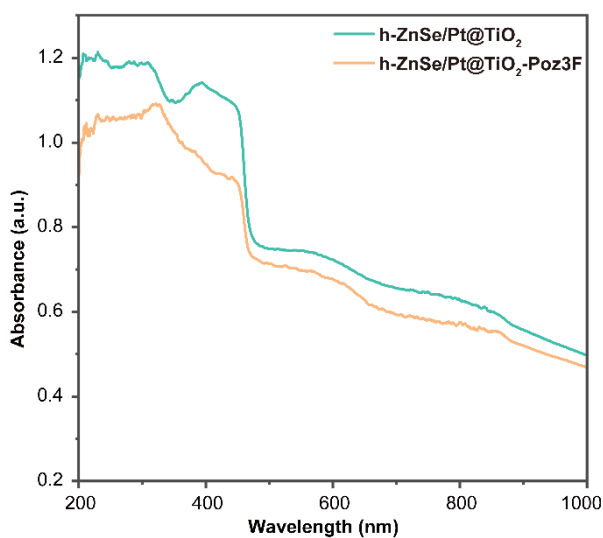


Figure S13. UV-vis spectra of h-ZnSe/Pt@TiO₂-Poz3F and h-ZnSe/Pt@TiO₂.

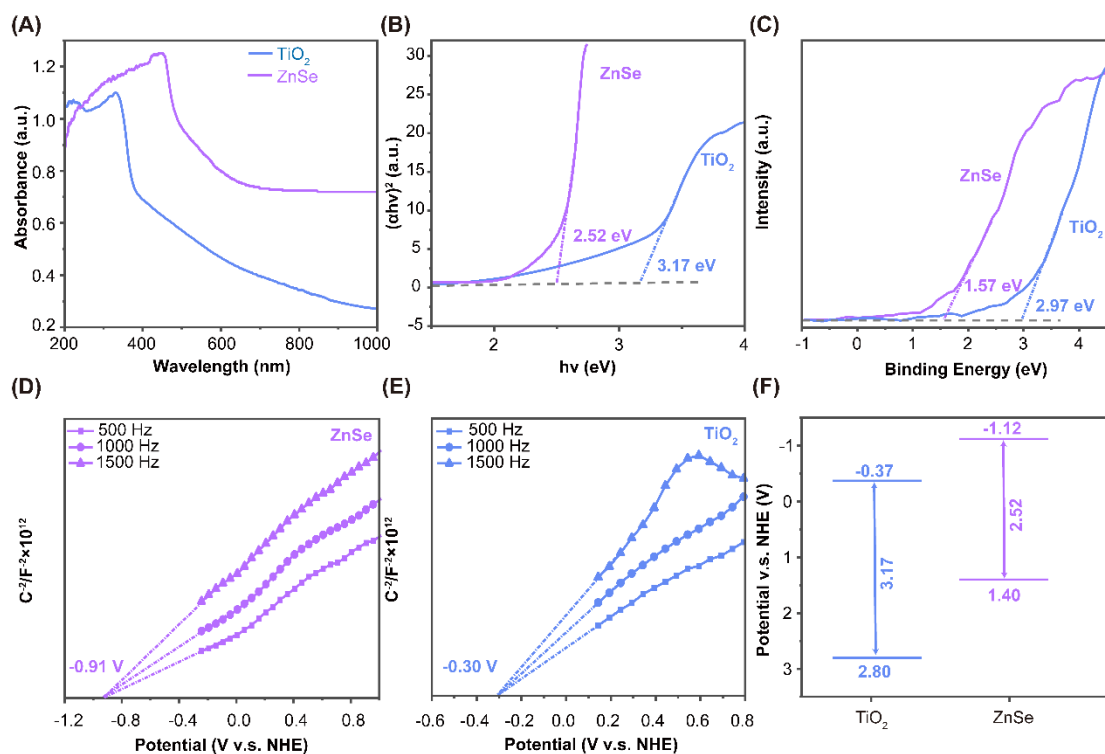


Figure S14. (A) DRS spectra, (B) plots of transformed Kubelka–Munk function versus photon energy, (C) VB-XPS, of ZnSe and TiO₂, respectively. (D) and (E) shows the Mott–Schottky plot of ZnSe and TiO₂, respectively. The band structure alignments estimated based on the UV-Vis and VB-XPS data are illustrated in (F).

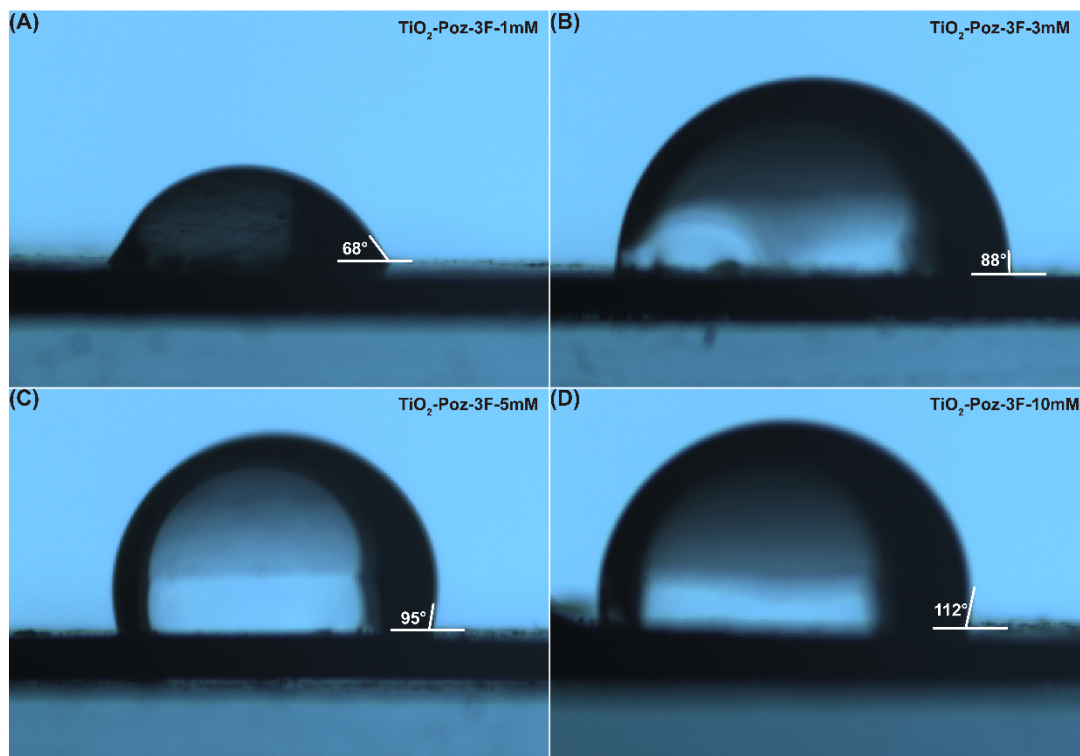


Figure S15. Photos of the contact angle measurements of samples treated in Poz3F with a concentration of (A) 1 mM, (B) 3mM, (C) 5 mM, and (D) 10 mM, respectively.

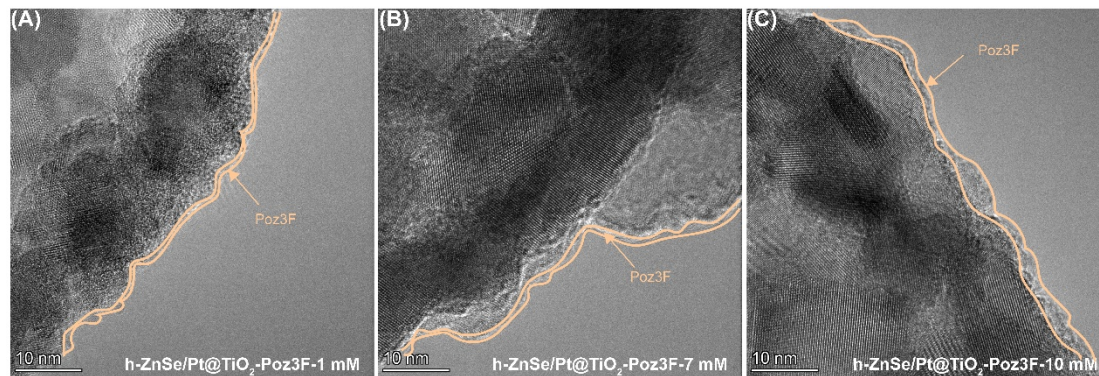


Figure S16. TEM images of samples treated in Poz3F with a concentration of (A) 1 mM, (B) 7 mM, and (C) 10 mM, respectively.

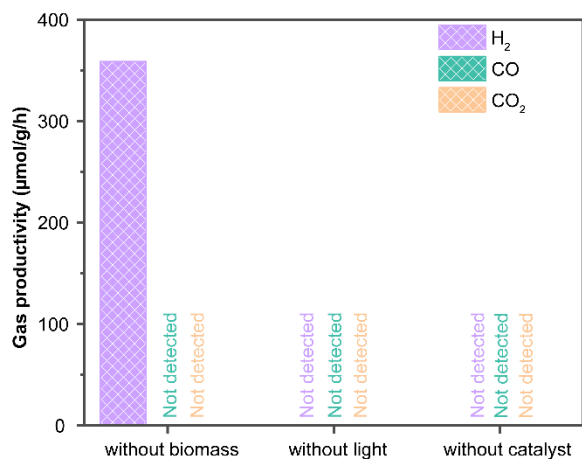


Figure S17. Gas productivity without biomass, light or photocatalyst.

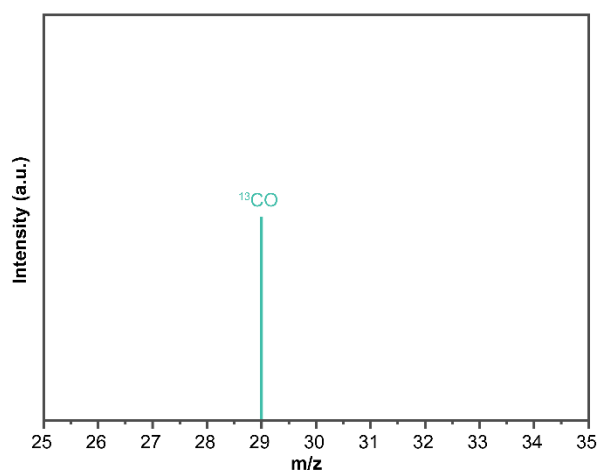


Figure S18. GC-MS of the isotopic tracing using ¹³C labeled glucose.

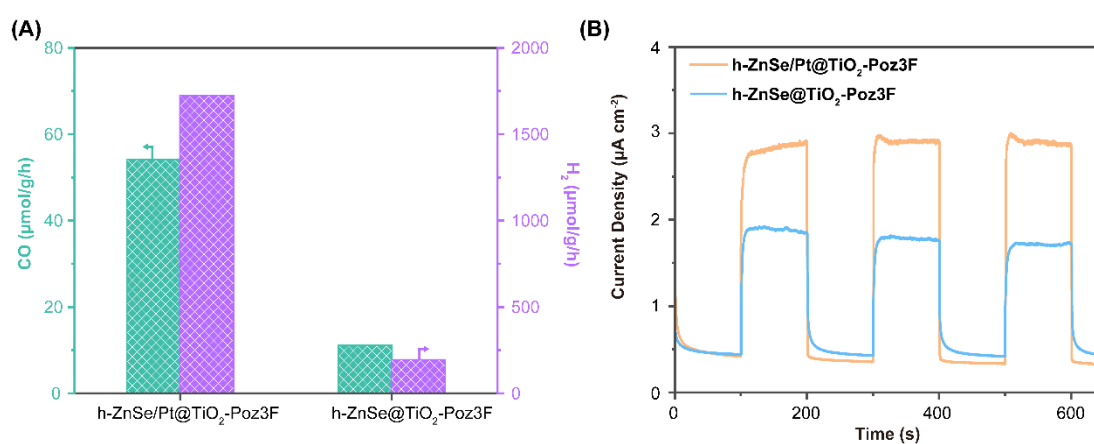


Figure S19. (A) H₂ and CO productivity using h-ZnSe/Pt@TiO₂-Poz3F and h-ZnSe@TiO₂-Poz3F. (B) Photocurrent measured with h-ZnSe/Pt@TiO₂-Poz3F and h-ZnSe@TiO₂-Poz3F.

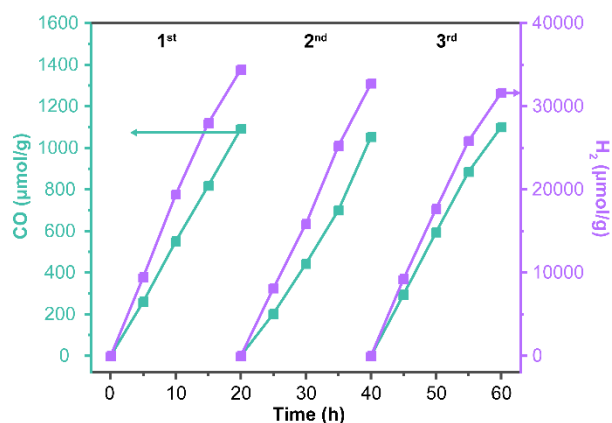


Figure S20. Photocatalytic cycling stability test of h-ZnSe/Pt@TiO₂-Poz3F.

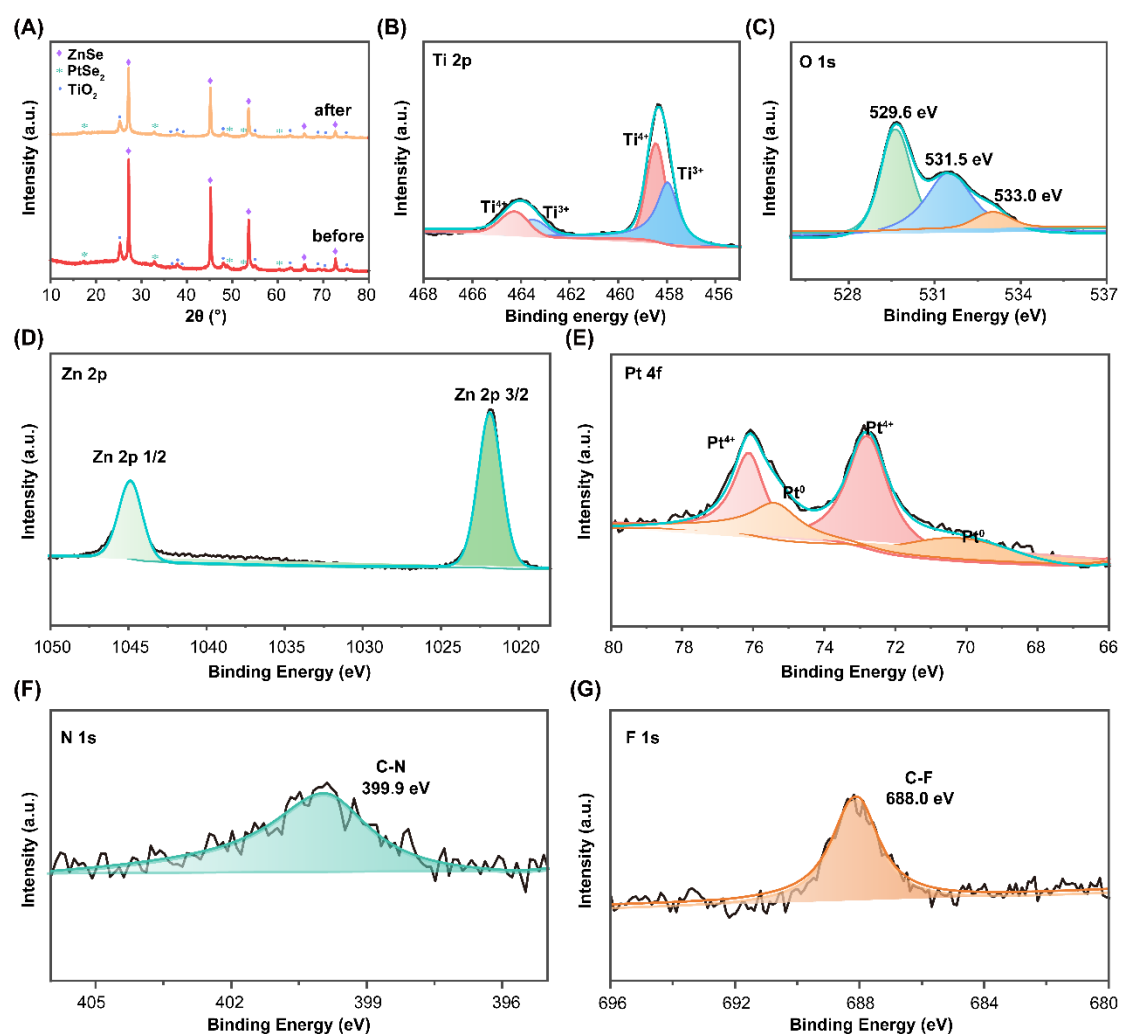


Figure S21. (A) Comparison of XRD patterns before and after photocatalysis. (B-G) Narrow scan XPS spectra of (B) Ti 2p, (C) O 1s, (D) Zn 2p, (E) Pt 4f, (F) N 1s and (G) F 1s for h-ZnSe/Pt@TiO₂-Poz3F after photocatalysis, respectively.

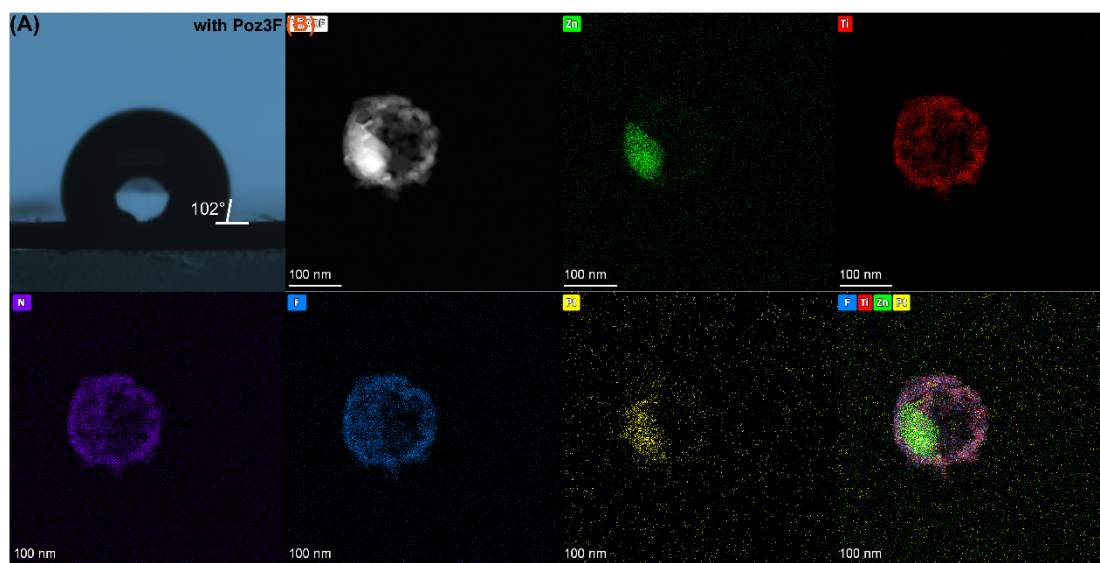


Figure S22. (A) Photo of contact angle measurement and (B) EDX element mapping images after photocatalysis, respectively.

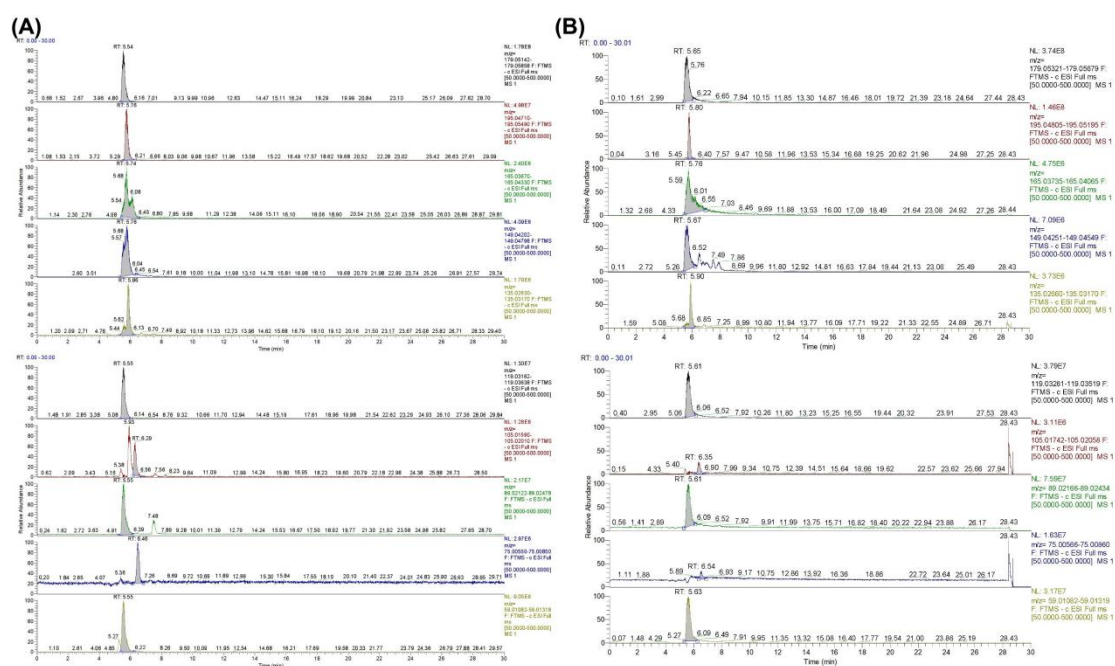


Figure S23. Extracted-ion chromatograms from the LC-MS analysis of deprotonated compounds in the after α -cellulose 2 hours irradiation solution with (A) h-ZnSe/Pt@TiO₂-Poz3F and (B) h-ZnSe/Pt@TiO₂, respectively.

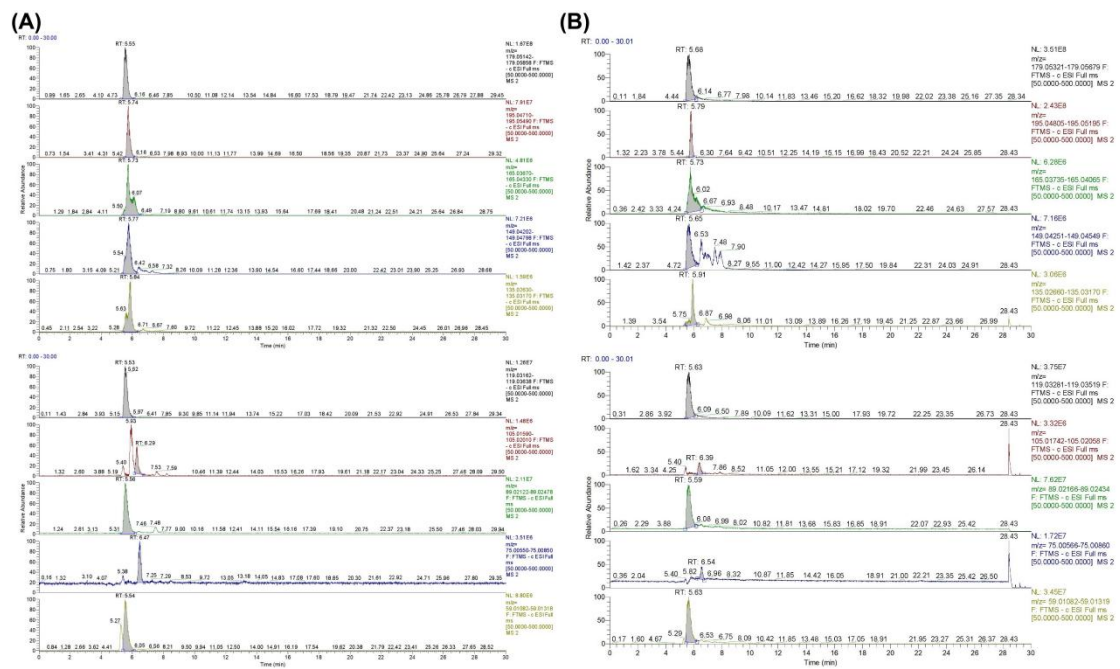


Figure S24. Extracted-ion chromatograms from the LC-MS analysis of deprotonated compounds in the after α -cellulose 6 hours irradiation solution with (A) h-ZnSe/Pt@TiO₂-Poz3F and (B) h-ZnSe/Pt@TiO₂, respectively.

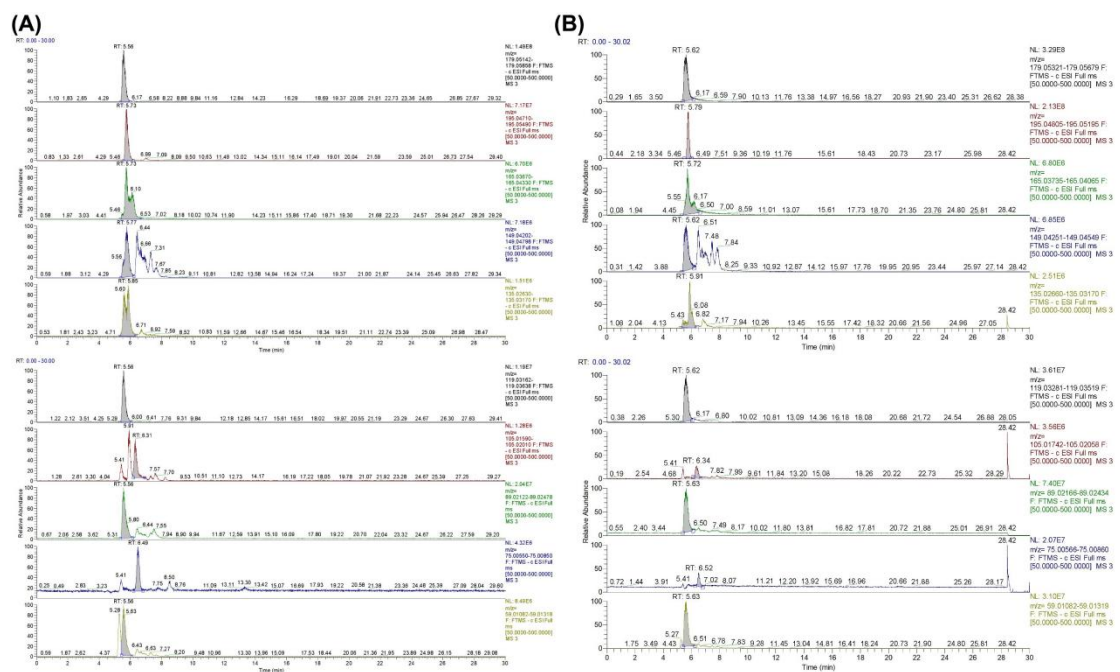


Figure S25. Extracted-ion chromatograms from the LC-MS analysis of deprotonated compounds in the after α -cellulose 18 hours irradiation solution with (A) h-ZnSe/Pt@TiO₂-Poz3F and (B) h-ZnSe/Pt@TiO₂, respectively.

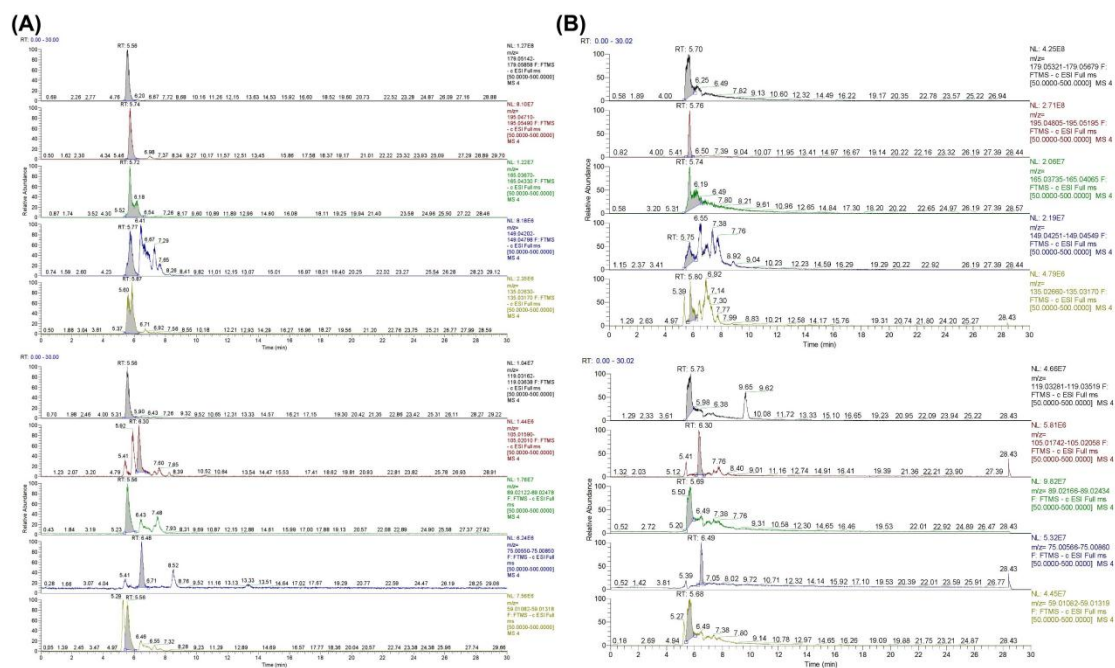


Figure S26. Extracted-ion chromatograms from the LC-MS analysis of deprotonated compounds in the after α -cellulose 48 hours irradiation solution with (A) h-ZnSe/Pt@TiO₂-Poz3F and (B) h-ZnSe/Pt@TiO₂, respectively.

Table S1. The content of Pt, Zn and Ti in h-ZnSe/Pt@TiO₂-Poz3F via ICP-MS.

	Pt	Zn	Ti
Content(%)	0.75	24.86	17.43

Table S2. Chemical formula and mass charge ratio of deprotonation compounds.

Chemical formular	Base peak m/z
$C_6H_{11}O_7$	195.04992
$C_6H_{11}O_6$	179.05521
$C_5H_9O_6$	165.03936
$C_5H_9O_5$	149.04436
$C_4H_7O_5$	135.02879
$C_4H_7O_4$	119.03372
$C_3H_5O_4$	105.01823
$C_3H_5O_3$	89.02311
$C_2H_3O_3$	75.00746
$C_2H_3O_2$	59.01256

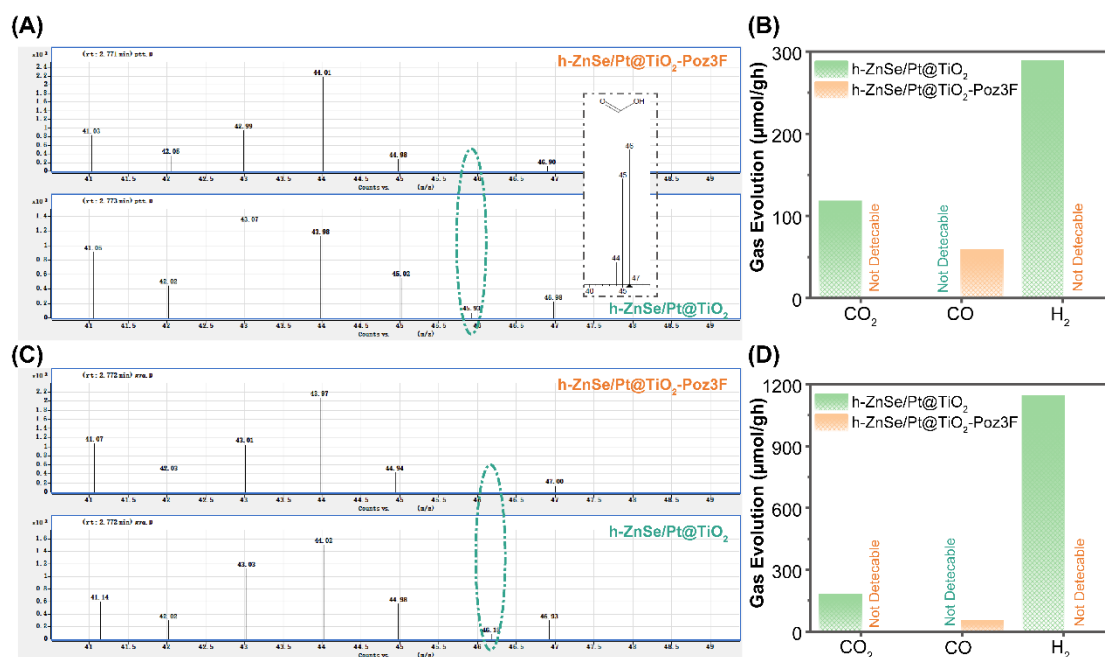


Figure S27. (A) GC-MS spectra (B) gas productivity after 10 min photocatalysis in glucose solution. (C) GC-MS spectra (B) gas productivity after 10 min photocatalysis in glyceraldehyde solution. The green ovals in (A) and (C) indicate the signal corresponding to formic acid in GC-MS. The inset in (A) is the standard GC-MS spectra

of formic acid.

To confirm the decarbonylation pathway, the gas and liquid phase products after only 10 min photocatalysis have been analyzed using glucose and glyceraldehyde as the substrates. As shown in Figure S18A and B, obvious CO production can be detected using h-ZnSe/Pt@TiO₂-Poz3F, while no signal for CO₂, H₂, and formic acid, further supporting the occurrence of decarbonylation pathway. In contrast, CO₂, H₂, and formic acid were produced in the early stage of photocatalysis using h-ZnSe/Pt@TiO₂, while no CO can be detected, indicating domination of decarboxylation pathway. These results further support that the Poz3F modification boost the decarbonylation pathway which is desired for CO production.

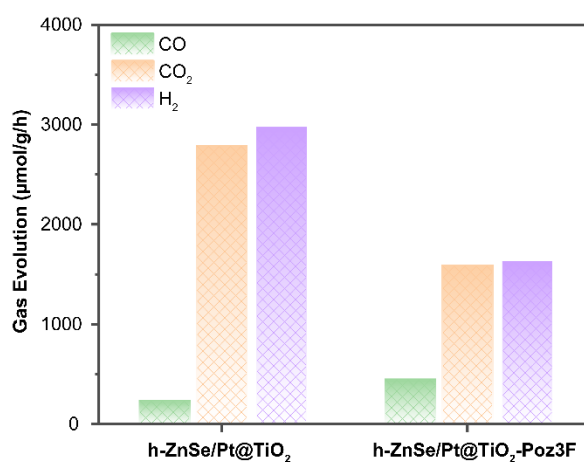


Figure S28. Formic acid reforming into CO, CO₂, H₂ productivity of ZnSe/Pt@TiO₂-Poz3F and h-ZnSe/Pt@TiO₂.

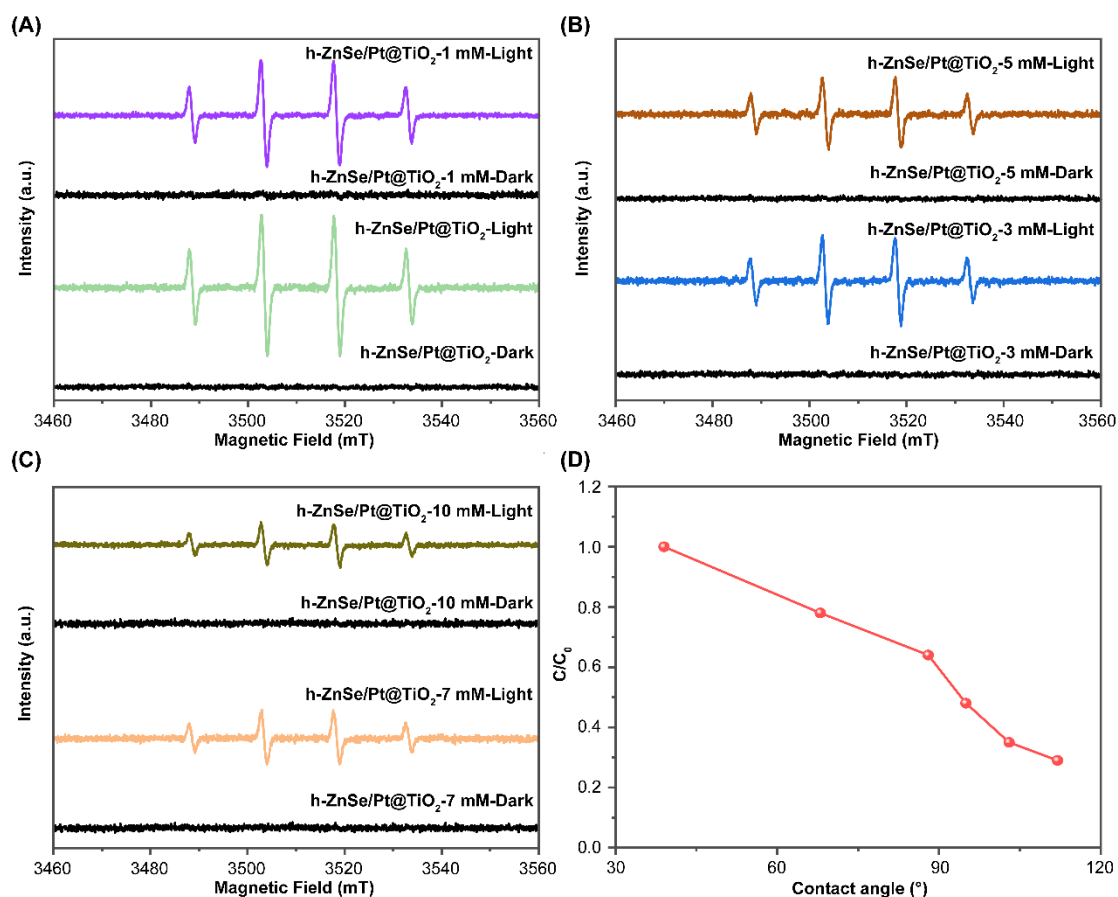


Figure S29. (A-C) EPR spectra of radical adducts signal labeled by DMPO for •OH generated by h-ZnSe/Pt@TiO₂-Poz3F prepared with different concentration of Poz3F. (D) Relationship between •OH generation and the measured contact angle.

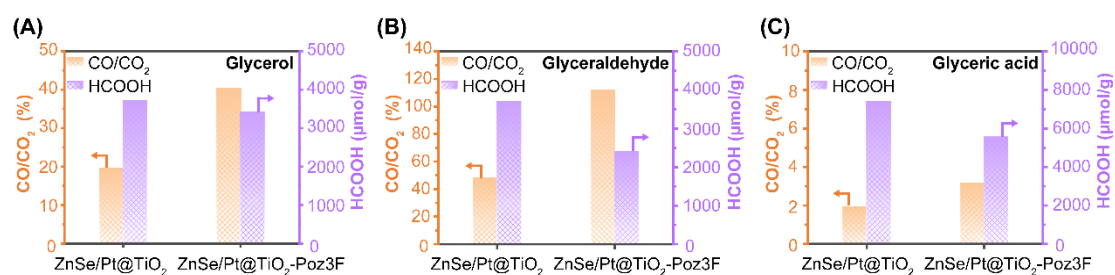


Figure S30. Comparison of CO/CO₂ ratio and formic acid productivity from (A) glycerol, (B) glyceraldehyde, and (C) glyceric acid using ZnSe/Pt@TiO₂-Poz3F and h-ZnSe/Pt@TiO₂, respectively.

References:

1. Kresse, G.; Joubert, D., From ultrasoft pseudopotentials to the projector augmented-wave method. *Physical Review B* **1999**, *59* (3), 1758-1775.
2. Perdew, J. P.; Burke, K.; Ernzerhof, M., Generalized Gradient Approximation Made Simple. *Physical Review Letters* **1996**, *77* (18), 3865-3868.
3. Grimme, S.; Antony, J.; Ehrlich, S.; Krieg, H., A consistent and accurate ab initio parametrization of density functional dispersion correction (DFT-D) for the 94 elements H-Pu. *The Journal of Chemical Physics* **2010**, *132* (15), 154104.
4. Monkhorst, H. J.; Pack, J. D., Special points for Brillouin-zone integrations. *Physical Review B* **1976**, *13* (12), 5188-5192.
5. Li, J.; Niu, L.; He, X., Enhanced visible-light activity of Ti³⁺ self-doped TiO₂ with co-exposed {001} and {101} facets. *Micro & Nano Letters* **2018**, *13* (4), 514-517.
6. Khan, M. M.; Ansari, S. A.; Pradhan, D.; Ansari, M. O.; Han, D. H.; Lee, J.; Cho, M. H., Band gap engineered TiO₂ nanoparticles for visible light induced photoelectrochemical and photocatalytic studies. *J. Mater. Chem. A* **2014**, *2* (3), 637-644.
7. Chen, W.; Li, X.; Wang, F.; Javaid, S.; Pang, Y.; Chen, J.; Yin, Z.; Wang, S.; Li, Y.; Jia, G., Nonepitaxial Gold-Tipped ZnSe Hybrid Nanorods for Efficient Photocatalytic Hydrogen Production. *Small* **2020**, *16* (12), e1902231.
8. Li, D.; Hussain, S.; Wang, Y.; Huang, C.; Li, P.; Wang, M.; He, T., ZnSe/CdSe Z-scheme composites with Se vacancy for efficient photocatalytic CO₂ reduction. *Applied Catalysis B: Environmental* **2021**, *286*, 119887.

